Heterogeneous InSAR Tropospheric Correction Based on Local Texture Correlation

Qingyue Yang, *Graduate Student Member, IEEE*, Zhang Yunjun, *Member, IEEE*,
and Robert Wang, *Senior Member, IEEE*

Abstract— Tropospheric delays have been a major limitation on the precision and accuracy of interferometric synthetic aperture radar (InSAR). InSAR phase-based tropospheric correction methods, especially the local window methods, could estimate heterogeneous tropospheric delays in the same resolution as InSAR data, thus, are increasingly desired for modern high-resolution InSAR products. However, the tropospheric phase–elevation relationship estimation at local windows can be severely contaminated by topography-correlated deformation. In this article, we present a new InSAR phase-based tropospheric correction method based on texture correlation between tropospheric delays and topography, which is shown to be relatively insensitive to topography-correlated deformation. The texture information represents the spatially high-frequency component of a 2-D image, which can be obtained using high-pass filtering. The method first produces a low-resolution tropospheric delay estimation using the window-wised texture correlation in the space domain, then refines it to high resolution by fitting the residual with the previously estimated tropospheric phase–elevation slope in the time domain. We apply the proposed method to ALOS-2 data over the Kirishima volcanic complex in Japan, encompassing typical topography-correlated deformation. The estimated phase–elevation slope shows seasonal oscillation in agreement with independent ERA5 prediction. The proposed method reduces the median spatial standard deviation (STD) of the residual phase from 0.7 to 0.4 cm, showing superior performance compared with other existing methods without compromising the deformation signal.

Index Terms— Interferometric synthetic aperture radar (InSAR), texture correlation, time series analysis, topography-correlated deformation, tropospheric delay.

I. Introduction

INTERFEROMETRIC synthetic aperture radar (InSAR) has emerged as a potent tool for monitoring surface deformation, owing to its ability to provide all-weather measurements with high resolution, rapid revisit, and wide area coverage [1]. The accuracy of InSAR displacement measure is limited by the decorrelation of the SAR signal, the atmospheric propagation delay, and the phase unwrapping error [2], [3], [4]. Among them, the tropospheric delay still remains as the major impediment that hinders the correct extraction and interpretation of deformation information from InSAR data. The intricate nature of tropospheric delays stems from various factors (e.g., temperature, pressure, relative humidity, and wind speed, etc. [5]), each with complex behaviors in both the time and space domains.

Spatially, the tropospheric delay includes stratified (systematic) and turbulent (stochastic) components; while temporally, it comprises seasonal (systematic) and nonseasonal (stochastic) components [6]. The stratified component demonstrates a correlation with topography and exhibits seasonal variations [6]. While the turbulent component exhibits stochastic behavior over time, with loss of correlation at one-day time intervals [7], and can be mitigated through filtering or long time-series averaging to some extent. The stratified tropospheric delay is the focus of this article.

Two categories of methods have been pursued to correct for tropospheric delays in InSAR data. The first category relies on external data or products, such as global atmospheric models [8], [9], [10], [11], [12], atmospheric water vapor from satellite spectrometers such as medium resolution imaging spectrometer (MERIS) and moderate resolution imaging spectroradiometer (MODIS) [6], [13], or from interpolating Global Navigation Satellite System (GNSS) observations [14], [15]. These methods may appear more dependable due to the integration of external data, but suffer from the limited temporal and spatial resolution of currently available external data products, which are in the tens of kilometer-scale, rendering them inadequate for modern high-resolution InSAR products [16]. The second category relies on the empirical relationship between tropospheric delays and InSAR phase, utilizing the phase–elevation relationship within the SAR scene on a global [17], local [5], [16], [18], [19], or multiscale [20], or exploiting the shared tropospheric contribution in redundant interferograms with common scenes [21], [22].

The spatial heterogeneity of tropospheric delays is one of the major challenges in tropospheric correction. The local-scale phase–elevation methods [16], [18], [19] could estimate parameters at the window or cluster level, making a solid step forward toward mapping heterogeneous tropospheric delays. However, the tropospheric phase–elevation relationship estimation at local scales is more severely affected by deformation, especially topography-correlated deformation, with a heightened risk of removing the deformation signal during
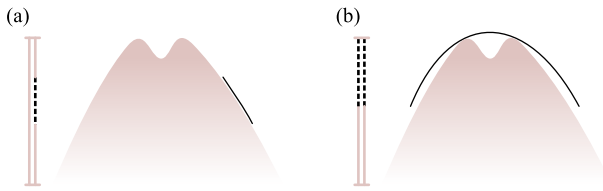
Fig. 1. Schematic of topography-correlated deformation. (a) Partially and (b) fully correlated deformation. The brown bump with a gradient color indicates the topography and black solid lines indicate deformation. Vertical lines on the left correspond to the elevation range of the topography, and black dashed lines correspond to elevation ranges occupied by deforming areas.

the fitting process, such as commonly seen in landslides [19] and active volcanoes [23] (as shown in Fig. 1). To mitigate this estimation bias, Wang et al. [19] identify points with large linear deformation rates and assign weights inversely proportional to the deformation rate (acting like a mask) through an iterative procedure, which works well with a low percentage of deforming pixels such as Fig. 1(a), but not with a high percentage of deforming pixels such as the truncated elevation range scenario as shown in Fig. 1(b), where the deformation covers the entire topographic peak, resulting in extrapolating the phase–elevation relationship, nor with nonlinear temporal deformation where the linear deformation rate is not representative anymore. Liang et al. [16] parameterize the tropospheric delay, deformation, and other phase components using empirical models and jointly solve for each model parameter, thus, could be inadequate for complex deformation scenarios and difficult to use in an operational system.

Built upon the multiscale spirit from Lin et al. [20], we present a new method to estimate the linear tropospheric phase–elevation slope using the texture [24] correlation between tropospheric delays and topography, which is shown to be relatively insensitive to deformation signal even at the local scale. Combining the texture correlation estimation with sliding local windows, we are able to estimate heterogeneous InSAR tropospheric delays with the presence of deformation. Unlike previous methods, we do not require masking nor rely on a comprehensive temporal deformation model.

In what follows, we first demonstrate the impact of deformation and tropospheric heterogeneity on the tropospheric phase–elevation estimation (see Section II). The detailed texture correlation-based tropospheric correction method is presented in Section III. We verify the method and evaluate its performance using data simulation in Section IV, then apply the method to the real data over Kirishima volcanoes, and compare it with other methods in Section V, followed by a discussion (see Section VI) and a conclusion (see Section VII).

II. TROPOSPHERIC PHASE–ELEVATION RELATIONSHIP

We examine here the impact of heterogeneity and deformation on the estimation of tropospheric phase and elevation relationship and examine the correlation between tropospheric delays and topography in the texture domain (spatial high-frequency band).

A. Tropospheric Phase–Elevation Linear Slope Estimation

The interferometric phase is composed of multiple components and can be expressed as

$$\mathbf{\Phi} = \mathbf{\Phi}_{\text{def}} + \mathbf{\Phi}_{\text{stra}} + \mathbf{\Phi}_{\text{ion}} + \mathbf{\Phi}_{\text{geom}} + \mathbf{\Phi}_{\text{tidal}} + \mathbf{\Phi}_{\varepsilon} \qquad (1)$$

where $\mathbf{\Phi}_{\text{def}}$ represents the deformation of the ground surface, which is usually the signal of interest, $\mathbf{\Phi}_{\text{stra}}$ represents the stratified tropospheric delay, which is the focus of this article. $\mathbf{\Phi}_{\text{ion}}$ represents the ionospheric propagation delay, which notably affects the long-wavelength phase component [25] and can be well estimated using the range split-spectrum method [26] or mitigated via deramping [27]. $\mathbf{\Phi}_{\text{geom}}$ represents the geometrical phase difference due to the nonzero spatial baseline between two acquisitions, including the topographic residual caused by the inaccurate digital elevation model (DEM), phase ramp due to orbit error, and possible phase ramp in the range direction due to timing error of SAR satellites, all can be well corrected using existing methods and models or ignored due to negligible contributions [28], [29], [30], [31]. $\mathbf{\Phi}_{\text{tidal}}$ represents long-wavelength contributions from tidal and loading effects and can be corrected using existing models [32], [33]. $\mathbf{\Phi}_{\varepsilon}$ represents the remaining contributions from decorrelation noise, nonclosure phase bias, system noise, processing errors, and tropospheric turbulence. After correcting for ionosphere, geometry, and tidal processes, (1) can be simplified as

$$\mathbf{\Phi} = \mathbf{\Phi}_{\text{def}} + \mathbf{\Phi}_{\text{stra}} + \mathbf{\Phi}_{\varepsilon}. \qquad (2)$$

The tropospheric turbulence may dominate $\mathbf{\Phi}_{\varepsilon}$ in the spatial domain, its significance diminishes when considering time series in the temporal domains.

The theoretical delay curve of a stratified troposphere model is an exponential function of the elevation, as the concentration of water vapor generally decreases exponentially with elevation [5]. The exponential function can be further simplified into a linear function within a certain elevation range [17], [34] as

$$\mathbf{\Phi}_{\text{stra}} = k\mathbf{H} + d \qquad (3)$$

where $\mathbf{H}$ is the elevation data matrix, k is the slope (linear coefficient), and d is the intercept. Since this linear relationship is satisfied within a certain elevation range, the linear fitting should be performed in local areas, which is also desired by the heterogeneity of the tropospheric delay.

When solving for k, it is usually assumed that the stratified tropospheric delay dominates the interferometric phase, then $\mathbf{\Phi}_{\text{stra}}$ can be substituted with $\mathbf{\Phi}$ in (2), then (3) can be rewritten as

$$[\hat{k}\ \hat{d}]^T = [\bar{\mathbf{H}}\ \mathbf{1}]^{\dagger}\bar{\mathbf{\Phi}} \qquad (4)$$

where the symbol "⁻" denotes the operation of converting a matrix to a column vector, $\mathbf{1}$ is a vector with all elements of 1 and the same size as $\bar{\mathbf{H}}$, and the symbols "T" and "$\dagger$" denote the transpose and pseudo-inverse operations on the matrix, respectively. If a deformation signal exists in the local area, i.e., $\mathbf{\Phi}_{\text{stra}}$ fails to satisfy the assumption of dominance, the estimation of the slope k will be distorted, resulting in biased estimations of tropospheric delays and deformation.

B. Impact of Tropospheric Heterogeneity and Deformation

We illustrate the impact of heterogeneity of tropospheric delays and deformation signals on the tropospheric phase–elevation relationship estimation in Fig. 2. For the tropospheric heterogeneity, we use multiple locations and sizes of estimation windows. In local windows at different locations [see Fig. 2(c) and (d)], a noticeable difference can be observed in the fit slopes, despite a mere separation of ∼5 km. The slope estimate also varies as the estimation window size changes from local to global scale [between Fig. 2(c)–(d) and (e)], despite sharing a common area, which is particularly evident for Iwo-yama. The relatively simple linear trend observed in the scatterplot at local windows becomes complicated in the global window, which is also commonly observed in other studies [9], [18]. Therefore, the phase–elevation-based correction with slopes estimated in the global scale is not representative of different local areas.

For the presence of deformation signals, we compare the estimated slopes with and without deformation masks [black and orange dashed lines in Fig. 2(c)–(e)]. It is evident that the fit slope, after masking the deformation region, aligns more consistently with the tropospheric phase–elevation relationship. This phenomenon is most pronounced in local estimation windows, that is, the smaller the estimation window, the more sensitive to deformation signals.

In summary, the traditional stratified tropospheric correction should be performed with a deformation mask and limited to local areas. However, the presence of topography-correlated deformation will very likely disable the masking operation at local scales, as the relationship between phase and elevation will be largely hidden [see Fig. 1(b)]. Furthermore, the presence of tropospheric turbulence could also easily break the dominance assumption of the stratified tropospheric delay at local scales. Therefore, a key issue arises in ensuring accurate stratified tropospheric correction within a local window while mitigating the interference caused by the topography-correlated deformation signal and tropospheric turbulence.

C. Texture Correlation

We examine the correlation between topography and tropospheric delays or deformation in both the regular space domain and the texture domain in Fig. 3. The texture referenced here is the spatially high-frequency component, which can be obtained through high-pass filtering. Here, we use a 2-D Gaussian filter with standard deviation (STD) of 180 m and size of 260 m for the texture calculation throughout this manuscript. Two cases are shown: one on the Karakuni volcano with simulated deformation [see Fig. 3(a)–(f)], one on the Shinmoe-dake volcano with observed deformation [see Fig. 3(g)–(l)], both uses observed tropospheric delays. For the two cases, the correlation between deformation and topography is comparable to the correlation between tropospheric delays and topography in the regular space domain [see Fig. 3(b)–(c) and (h)–(i)]. While in the texture domain, the correlation between deformation and topography is significantly attenuated, and the correlation between tropospheric delays and topography becomes noticeably stronger relatively
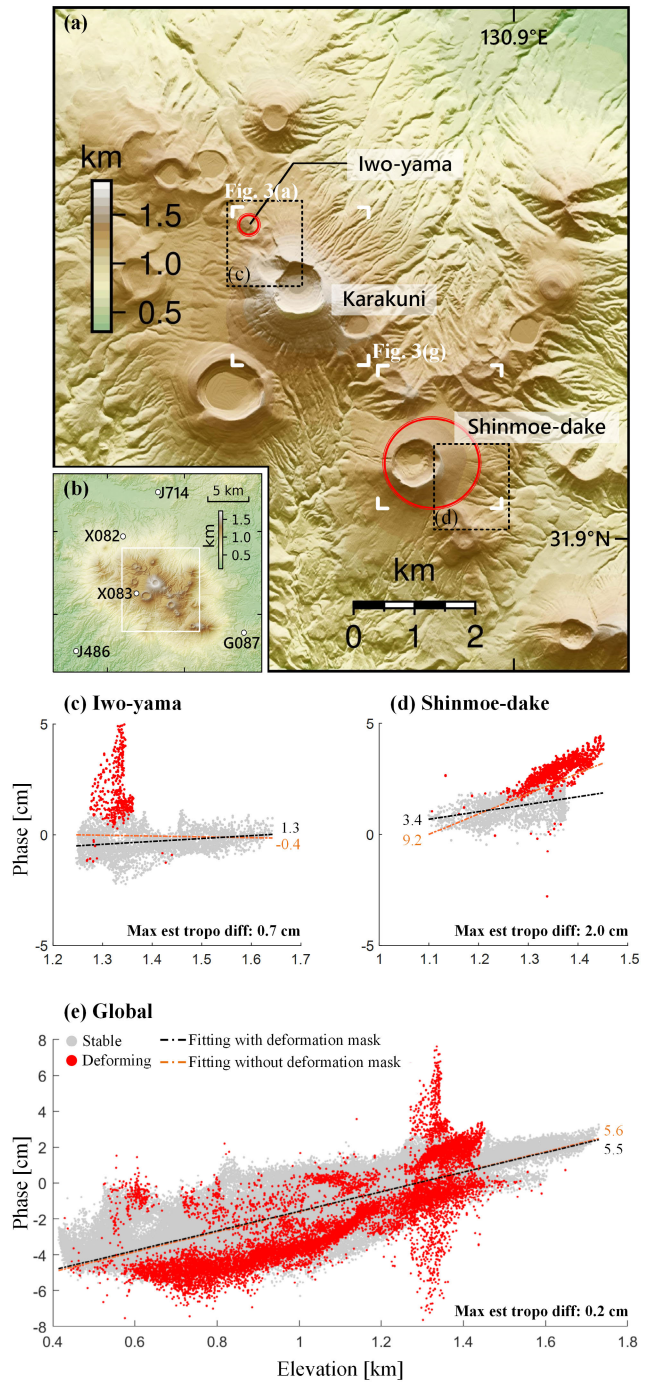

Fig. 2. Impact of tropospheric heterogeneity and deformation on the tropospheric phase–elevation slope estimation, using an ALOS-2 interferogram from descending track 23 acquired between February 23, 2015 and November 14, 2016 covering the Kirishima volcanic complex, Japan (see Section V-A for detailed descriptions). (a) DEM of the Kirishima volcanic complex in UTM coordinates. Red circles: deforming areas as identified in [35]. (b) DEM of the expanded study area. White box: scope of (a). Black circles: GNSS stations. (c) and (d) Scatterplots of the phase–elevation with/without deformation mask within two local windows (black dashed boxes in (a), 71 × 71 pixels, ∼1.4 × 1.2 km) covering Iwo-yama and part of Shinmoe-dake volcanoes, respectively. (e) Same as (c) for the entire study area (541 × 541 pixels, ∼10.8 × .2 km). Black and orange dashed lines: fitting slopes in cm/km with/without applying a deformation mask, respectively.

[see Fig. 3(e)–(f) and (k)–(l)]. Here, we refer spatial correlation and texture correlation as the correlation between the phase
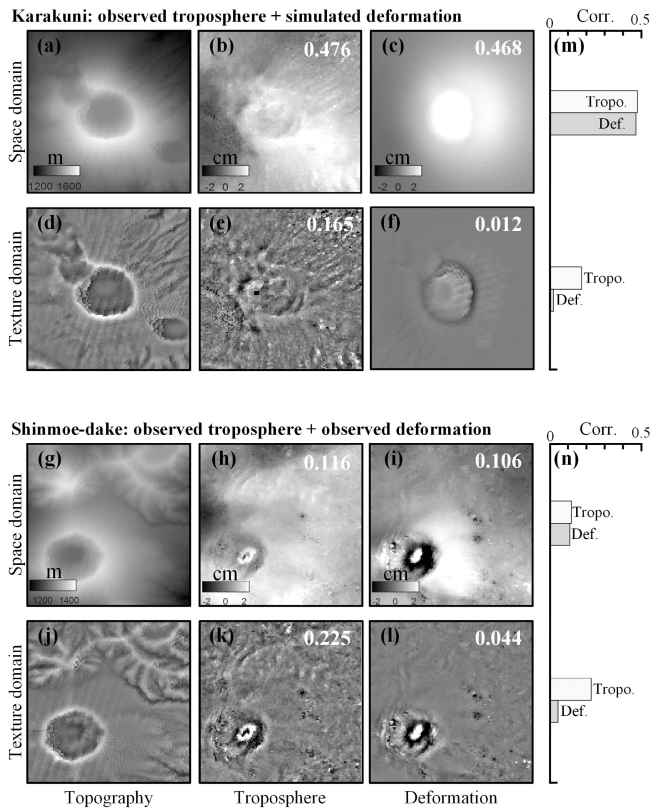
Fig. 3. Spatial and texture correlation among topography, tropospheric delays, and deformation. (a)–(f) Karakuni volcano [marked by white right angles in Fig. 2(a)]. (a) Topography. (b) ALOS-2 interferogram (February 23, 2015 and September 18, 2017, see Section V-A for details) dominated by tropospheric delays. (c) Simulated deformation using the same parameters of the pre-eruptive inflation of the 2017 Shinmoe-dake eruption [35], [36], [37]. (d)–(f) Texture maps of (a)–(c). White numbers: correlation coefficients between tropospheric delays or deformation and topography in space and texture domain. (g)–(l) Same as (a)–(f) but for Shinmoe-dake volcano, using an interferogram from February 23, 2015 and September 21, 2015 for tropospheric delays (with deformation removed using estimated deformation rate), and the observed deformation from estimated deformation rate. (m) and (n) Correlation coefficients of tropospheric delays or deformation with topography in the space and texture domains in bar graph styles.

(of any component) and the topography in the space and texture domain, respectively.

Note that the weak spatial correlation of 0.1 between deformation and topography [see Fig. 3(i)] could still bias the tropospheric estimation using local linear fitting method, as shown in Fig. 2(d). And this weak spatial correlation is not uncommon in volcanoes (dike intrusion, asymmetric volcanic inflation, etc.) and landslides. The correlation reduced from space to texture domain in all four cases, except for Fig. 3(h) and (k), where the correlation increased. The former can be explained by the weakened signal to the high-frequency noise ratio due to the reduced signal magnitude from the high-pass filtering, while the latter can be explained by the enhanced ratio due to the weakened influence of tropospheric turbulence from the high-pass filtering.

The relatively stronger texture correlation between tropospheric delays and topography compared to that between deformation and topography is probably because the magnitude variation of deformation (due to subsurface processes)
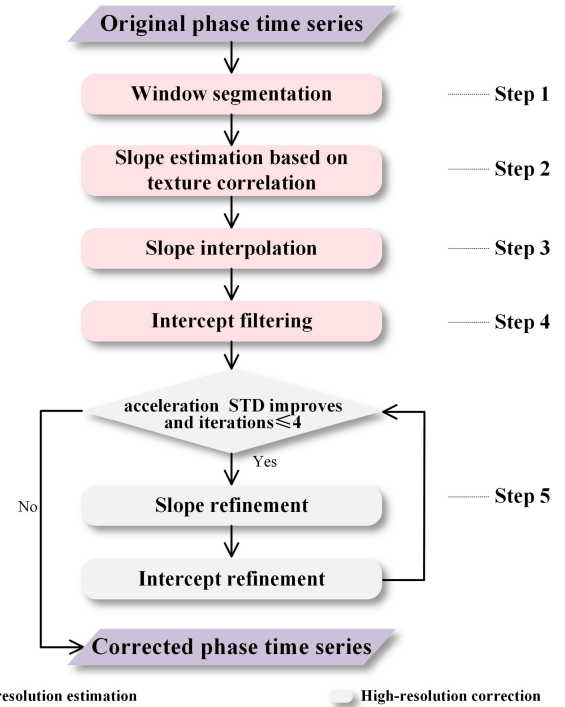

Fig. 4. Flowchart of the proposed method. Steps 1–4 form the low-resolution stratified tropospheric estimation module, and step 5 forms the high-resolution stratified tropospheric correction module.

is not or weakly related to the relief of the topography, while the magnitude variation of tropospheric delays is tightly related to the relief of surface topography. Therefore, there is a high potential to remove stratified tropospheric delays with the presence of topography-correlated deformation using the texture correlation between phase and topography.

III. METHODOLOGY

We present a phase-based method to estimate heterogeneous stratified tropospheric delays with the presence of topography-correlated deformation. The method includes two modules.

1) A low-resolution stratified tropospheric estimation module relying on linear relationship between stratified tropospheric delays and elevation, which primarily conducts window-by-window slope estimation based on texture correlation. This module assumes that the texture of topography-correlated deformation and tropospheric turbulence exhibits weak or no correlation with that of the topography.

2) A high-resolution stratified tropospheric correction module, mainly implemented in the time domain, to address the intrawindow heterogeneity. This module assumes that deformation is not correlated with the tropospheric phase–elevation slope in the temporal high-frequency component.

The workflow is summarized in Fig. 4 with example outputs for each step shown in Fig. 5, and can be described as follows.

Step 1: Window segmentation based on the guidelines described in Section III-A for the size and spacing.

Step 2: Window-wised slope estimation based on texture correlation using (8).
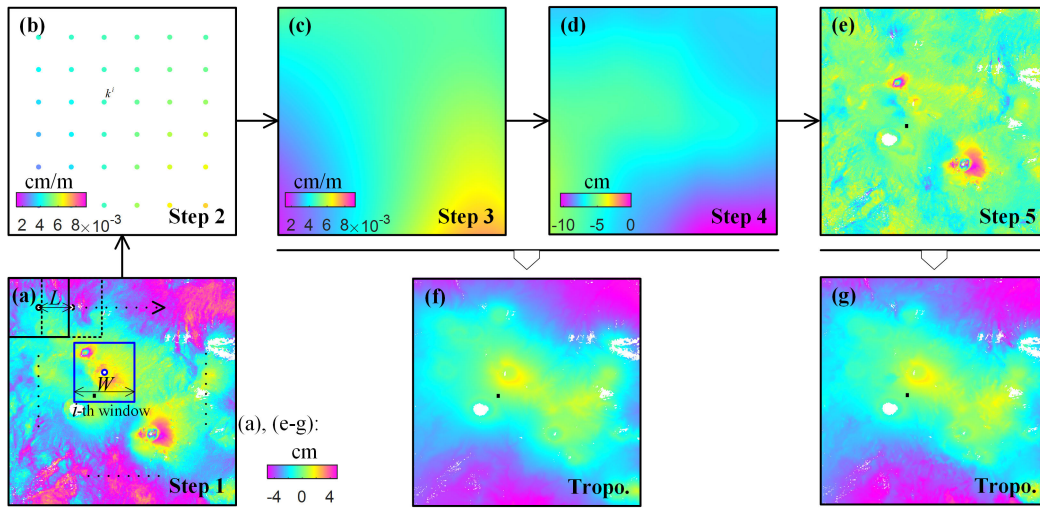
Fig. 5. Processing flow using an example ALOS-2 interferogram (February 3, 2015 and August 21, 2017 from Section V-A). (a)–(e) Direct results of steps 1–5 in the flowchart shown in Fig. 4, respectively, where (a) is the original interferogram, (b) is the discrete slopes estimated window-by-window after low-pass filtering, (c) is the slope map after interpolating (b), (d) is the intercept map obtained by intercept filtering, and (e) is the final corrected interferogram after high-resolution stratified tropospheric correction. (f) and (g) Estimated stratified tropospheric delay obtained from the low- and high-resolution stratified tropospheric estimation module, respectively. Black squares: reference points. Data are rewrapped into [−5, 5) cm for display.

Step 3: Slope interpolation using (5).

Step 4: Intercept filtering using (6).

Step 5: Iterative slope and intercept refinements based on (13), (17), and (18) until reach the limited number of iterations as described in Section III-B.

A. Low-Resolution Stratified Tropospheric Estimation via Local Texture Correlation

The purpose of the low-resolution stratified tropospheric estimation module is to estimate the initial 2-D slope map (denoted as matrix $\hat{\mathbf{K}}$) and intercept map (denoted as matrix $\hat{\mathbf{D}}$) of phase–elevation relationship for each interferogram. Since the estimation is executed in local windows to account for the tropospheric heterogeneity, a local phase–elevation slope is obtained based on texture correlation in each window, i.e., the slope estimated in the ith window centered at coordinate s^i is $\hat{k}^i$ and $\hat{k}^i = \hat{\mathbf{K}}|_{s=s^i}$. After the window-by-window estimation, a slope grid with discrete distribution over the 2-D space is obtained, and a low-pass filtering (the filter window size is denoted as w_k) is employed to align the spatial correlation length of the 2-D slope with that of the subsequently estimated intercept (explained in more detail in Section III-A2). Then the coarse slope grid is interpolated to the entire space to obtain the complete 2-D slope map $\hat{\mathbf{K}}$. Given the moving window samples points $I_r \times I_c$, the process can be expressed as

$$\left[\hat{\mathbf{K}} \right]_{I_r \times I_c, \text{LP}} \xrightarrow{\text{interp}} \hat{\mathbf{K}}$$
$$\hat{k}^i \in \hat{\mathbf{K}}_{I_r \times I_c}, \quad i = 1, \ldots, I_r \times I_c \quad (5)$$

where the symbol $[*]_{\text{LP}}$ denotes the operation of low-pass filtering. Additionally, the estimation window size [denoted as W and illustrated with a square window in Fig. 5(a)] should be selected to balance two factors: spatial heterogeneity calls for a small window, while rich texture information required for estimation demands a larger one. Therefore, we should

minimize the window size under the premise that the texture required for estimation are rich enough.

Next, the intercept $\hat{\mathbf{D}}$ can be estimated based on the slope map $\hat{\mathbf{K}}$ and the original phase $\boldsymbol{\Phi}$. With the presence of topography-correlated deformation, the deformation signal is inevitably smoothed out when the intercept is estimated within a local window according to the conventional method, i.e., (4). Therefore, we simply use low-pass filtering to estimate $\hat{\mathbf{D}}$, called intercept filtering hereafter, that is,

$$\hat{\mathbf{D}} = \left[\boldsymbol{\Phi} - \hat{\mathbf{K}} \cdot \mathbf{H} \right]_{\text{LP}} \quad (6)$$

where low-pass filtering with a relatively large window (compared with deformation range, and the filter window size is denoted as w_d) is applied to avoid the contamination of topography-correlated deformation, which limits this module to obtaining only the low-resolution stratified tropospheric estimation. Note that a phase ramp in the InSAR data could potentially bias the intercept filtering result, this can be easily mitigated by first estimating and removing this phase ramp before tropospheric correction and add them back after the correction.

The deformation phase after the low-resolution stratified tropospheric correction is obtained as

$$\hat{\boldsymbol{\Phi}}_{\text{def}} = \boldsymbol{\Phi} - \left(\hat{\mathbf{K}} \cdot \mathbf{H} + \hat{\mathbf{D}} \right) \quad (7)$$

where $\hat{\mathbf{K}} \cdot \mathbf{H} + \hat{\mathbf{D}}$ is the estimated low-resolution stratified tropospheric delay. The above is the general flow of the low-resolution stratified tropospheric estimation module, below we describe the detailed process to estimate the slope for each window, and to select estimation-related parameters.

1) Texture Correlation-Based Local Slope Estimation: For each local estimation window, the slope $\hat{k}^i$ is determined based on texture correlation. Under the assumption that the texture of topography-correlated deformation and tropospheric turbulence exhibits weak or no correlation with that of the topography, the slope can be obtained through tuning $\hat{k}^i$ until

the texture correlation between $\mathbf{\Phi}^i - \hat{k}^i \mathbf{H}^i$ (the superscript i of the matrix denotes the submatrix bounded by the ith window) and topography $\mathbf{H}^i$ reaches the minimum as

$$\hat{k}^i = \arg \min_{\hat{k}^i} \frac{\left|\left[\mathbf{\Phi}^i - \hat{k}^i \mathbf{H}^i\right]_{\mathrm{HP}} \cdot \left[\mathbf{H}^i\right]_{\mathrm{HP}}\right|}{\left|\left[\mathbf{\Phi}^i - \hat{k}^i \mathbf{H}^i\right]_{\mathrm{HP}}\right|\left|\left[\mathbf{H}^i\right]_{\mathrm{HP}}\right|} \quad (8)$$

where the symbol $[*]_{\mathrm{HP}}$ denotes the operation of high-pass filtering to extract the texture information, and the symbol $|*|$ calculates the module of the matrix after converting into a column vector. An initial value of $\hat{k}^i$ can be obtained based on the phase–elevation relationship within the ith window using (4) to save the search time of the solution. Optionally, one may mask out the localized deformations with large magnitudes, which can be recognized from low-precision deformation rate map, such as calculated from the original phase time series, together with a outlier detection algorithm, to avoid unnecessary errors caused by the possible interference of its high-frequency component, however this is generally not required. Note that since the phase–elevation relationship is not directly linear in the high-frequency band [20], the linear fitting cannot be adopted to solve for $\hat{k}^i$ here.

2) Guidance on Parameter Selection: As for the window size for slope estimation, given that our foremost priority is ensuring the accuracy of estimation within the deformation region, the window is configured to ensure evident topography texture as it slides through the deformation region. The spacing or step size of the estimation window L, which controls the spatial density of the estimated slopes, is recommended to ensure the window overlap rate greater than 40% to avoid over extrapolation of data during the slope interpolation step. Finally, for parameters related to the slope and intercept filtering, we analogously match the spatial correlation length of the slope to that of the intercept. This can be approximated by the following expression: $w_d \leq (w_k - 1)L$ and $w_d \geq (w_k - 1)L/2$. In summary, the parameters are determined in the following order: setting W according to the texture of topography in the deformation region, setting L according to the window overlap rate, setting w_d according to the range of deformation (obtained from low-precision deformation rate map), and setting w_k according to w_d and L.

B. High-Resolution Stratified Tropospheric Correction via Temporal Fitting

The purpose of the high-resolution module is to correct for the residual stratified tropospheric delay due to intrawindow heterogeneity, which is performed in the time domain for each point to obtain the corrected time series with high-resolution stratified tropospheric delays removal. As a general illustration, we use s to represent an arbitrary point in space. Consider a total of N SAR images, the original phase time series can be noted as $\boldsymbol{\phi} = [\phi^1, \ldots, \phi^n, \ldots, \phi^N]^T$, where the subscript n denotes the nth acquisition and $\phi^n = \mathbf{\Phi}^n|_s$. Analogously, we can get $\boldsymbol{\phi}_\varepsilon$, $\boldsymbol{\phi}_{\mathrm{def}}$, $\hat{\boldsymbol{\phi}}_{\mathrm{def}}$, $\boldsymbol{k}$, $\boldsymbol{d}$, $\hat{\boldsymbol{k}}$, $\hat{\boldsymbol{d}}$ and h, where $\boldsymbol{k}$ and $\boldsymbol{d}$ are the true slopes and intercepts at point s, respectively. Then, in the 1-D time domain at s, (2) and (3) can be rewritten as

$$\boldsymbol{\phi} = \boldsymbol{\phi}_{\mathrm{def}} + h\boldsymbol{k} + \boldsymbol{d} + \boldsymbol{\phi}_\varepsilon \quad (9)$$

and (7) can be rewritten as

$$\hat{\boldsymbol{\phi}}_{\mathrm{def}} = \boldsymbol{\phi} - \left(h\hat{\boldsymbol{k}} + \hat{\boldsymbol{d}}\right)$$
$$= \boldsymbol{\phi}_{\mathrm{def}} + h\left(\boldsymbol{k} - \hat{\boldsymbol{k}}\right) + \left(\boldsymbol{d} - \hat{\boldsymbol{d}}\right) + \boldsymbol{\phi}_\varepsilon. \quad (10)$$

Given that the stratified tropospheric delay is spatially correlated, the interpolated slope time series $\hat{\boldsymbol{k}}$ at s, while not identical to the true slope time series $\boldsymbol{k}$, is correlated with $\boldsymbol{k}$. Then further assume that at s, $\boldsymbol{k} = \alpha\hat{\boldsymbol{k}} + \boldsymbol{\varepsilon}$, where α is an unknown constant coefficient and $\boldsymbol{\varepsilon}$ is a 1-D time series used for compensating for the portion of $\boldsymbol{k}$ uncorrelated with $\hat{\boldsymbol{k}}$, so there yields

$$\hat{\boldsymbol{\phi}}_{\mathrm{def}} = \boldsymbol{\phi}_{\mathrm{def}} + h\left[\left(\alpha\hat{\boldsymbol{k}} + \boldsymbol{\varepsilon}\right) - \hat{\boldsymbol{k}}\right] + \left(\boldsymbol{d} - \hat{\boldsymbol{d}}\right) + \boldsymbol{\phi}_\varepsilon$$
$$= \boldsymbol{\phi}_{\mathrm{def}} + h\left[(\alpha - 1)\hat{\boldsymbol{k}} + \boldsymbol{\varepsilon}\right] + \left(\boldsymbol{d} - \hat{\boldsymbol{d}}\right) + \boldsymbol{\phi}_\varepsilon$$
$$= \boldsymbol{\phi}_{\mathrm{def}} + \eta\hat{\boldsymbol{k}} + \boldsymbol{d}_\varepsilon + \boldsymbol{\phi}_\varepsilon \quad (11)$$

where the constant coefficient $h(\alpha - 1)$ is replaced by the symbol η, and the time series $h\boldsymbol{\varepsilon} + (\boldsymbol{d} - \hat{\boldsymbol{d}})$ is replaced by the symbol $\boldsymbol{d}_\varepsilon$. Thus, the objective of this module is to attenuate the last three terms of (11), bringing $\hat{\boldsymbol{\phi}}_{\mathrm{def}}$ closer to $\boldsymbol{\phi}_{\mathrm{def}}$.

1) Time Function Fitting: To prevent the linear deformation rate from interfering with the solution of η, we assume a linear temporal deformation model for $\boldsymbol{\phi}_{\mathrm{def}}$. This is similar to the model-based DEM error estimation [28], which estimates the contribution correlated with the perpendicular baseline time series. Then, (11) can be rewritten as

$$\hat{\boldsymbol{\phi}}_{\mathrm{def}} = v\mathbf{t} + c + \eta\hat{\boldsymbol{k}} + \boldsymbol{d}_\varepsilon + \boldsymbol{\phi}_\varepsilon \quad (12)$$

where v is the velocity, c is a constant offset, $\mathbf{t}$ is the SAR acquisition time vector. And η can be estimated by least squares as follows:

$$\begin{bmatrix} v & c & \eta \end{bmatrix}^T = \begin{bmatrix} \mathbf{t} & \mathbf{1} & \hat{\boldsymbol{k}} \end{bmatrix}^\dagger \hat{\boldsymbol{\phi}}_{\mathrm{def}}. \quad (13)$$

The simple linear deformation model can be replaced with a more complex suite of time functions, such as higher order polynomial, periodic, and step functions [39]. However, as we are interested in the estimation of the constant η, the assumed deformation model does not need to be comprehensive.

2) Iteration: We assume that the variation in rate of deformation events unfold in nature with continuity. While acknowledging the potential for abrupt changes, we regard them as incidental. This corresponds to a small STD of acceleration, which can be described as

$$\sigma(\boldsymbol{f}) = \sqrt{\frac{\sum_{n=2}^{N-1}\left(a^n - \bar{a}\right)^2}{N - 2}} \quad (14)$$

where

$$a^n = \frac{2\left(\frac{f^{n+1} - f^n}{t^{n+1} - t^n} - \frac{f^n - f^{n-1}}{t^n - t^{n-1}}\right)}{t^{n+1} - t^{n-1}} \quad (15)$$

$$\bar{a} = \sum_{n=2}^{N-1} \frac{a^n}{N - 2} \quad (16)$$

and $\boldsymbol{f}$ represents an arbitrary 1-D time series signal. We use the improvement of σ as the trigger condition to govern the update of $\hat{\boldsymbol{\phi}}_{\mathrm{def}}$, i.e., if $\sigma(\hat{\boldsymbol{\phi}}_{\mathrm{def}} - \eta\hat{\boldsymbol{k}}) < \sigma(\hat{\boldsymbol{\phi}}_{\mathrm{def}})$, the

following is executed: subtract $\eta\hat{\boldsymbol{k}}$ from $\hat{\boldsymbol{\phi}}_{\text{def}}$, perform the intercept filtering with window size w_d to obtain the new $\hat{\boldsymbol{\phi}}_{\text{def}}$, which can be written as

$$\hat{\boldsymbol{\phi}}_{\text{def}}(\text{new}) = \hat{\boldsymbol{\phi}}_{\text{def}} - m\eta\hat{\boldsymbol{k}}$$
$$\hat{\boldsymbol{\phi}}_{\text{def}} = \hat{\boldsymbol{\phi}}_{\text{def}}(\text{new}) \tag{17}$$
$$\hat{\Phi}_{\text{def}}^n(\text{new}) = \hat{\Phi}_{\text{def}}^n - \hat{\mathbf{D}}$$
$$= \hat{\Phi}_{\text{def}}^n - \left[\hat{\Phi}_{\text{def}}^n \cdot \mathbf{M}\right]_{\text{LP}} \cdot \mathbf{M}, \quad n = 1, \ldots, N$$
$$\hat{\Phi}_{\text{def}}^n = \hat{\Phi}_{\text{def}}^n(\text{new}) \tag{18}$$

where $\mathbf{M}$ records the satisfaction of the trigger condition for each spatial location, 1 means satisfied while 0 means not, and $m = \mathbf{M}|_s$. Using this indicator assumes that the deformation $\boldsymbol{\phi}_{\text{def}}$ is not correlated with the estimated tropospheric slope $\hat{\boldsymbol{k}}$ in temporal high-frequency component.

Regarding (17) and (18), there are two additional details to note at the processing level: one involves spatial filtering of η to eliminate high-frequency noise, and the other involves smoothing the phase jump boundary between the updated and un-updated pixel regions caused by $\mathbf{M}$ multiplication on $[\hat{\Phi}_{\text{def}}^n \cdot \mathbf{M}]_{\text{LP}}$. In Fig. 4, operations represented by (17) and (18) are referred to as slope refinement and intercept refinement, respectively. We iterate this process up to four times to improve the accuracy of the estimation.

IV. SIMULATED DATA EXPERIMENTS

We verify the effectiveness of the texture correlation method using data simulation and analyze the impact of the estimation window size on the performance of the method. Since our focus here is evaluate the capability of the method to separate tropospheric delays in the texture domain, only the low-resolution estimation module using texture correlation from Section III-A is applied.

A. Simulation Setting

We simulate interferometric phases of the Kirishima volcanic complex, Japan considering contributions from deformation, stratified tropospheric delays and tropospheric turbulence, as shown in Fig. 6(a)–(d). More specifically, we simulate the surface deformation using the same parameters of the pre-eruptive inflation of the 2017 Shinmoe-dake eruption [35], [36]. The impact of topography is included following Williams and Wadge [37]. The stratified tropospheric delay is grabbed from ERA5 [40] of the ALOS-2 time series in Section V. The tropospheric turbulence is modeled as an isotropic 2-D surface with a power law behavior [3], [38] with a fixed slope of 8/3 and reference power spectrum density calculated from the residual phase of the ALOS-2 time series in Section V, which has been corrected for troposphere using ERA5 and deformation using a quadratic polynomial time function.

For the texture correlation, we set the intercept filtering window size to 201 pixels ($\sim$4.0 km) according to the range of the deformation region, with a 65% overlap between windows. The window size for slope filtering is set according to the guidance in Section III-A. In Fig. 6(e), we use a window size of 196 pixels ($\sim$3.9 km) for the texture correlation calculation.

B. Performance of Separating Tropospheric Delays

To evaluate the performance of the proposed method in separating tropospheric delays from topography-correlated deformation, we calculate the median absolute error and median absolute deviation (MAD) of the estimated tropospheric delay in the deforming region [dotted rectangle in Fig. 6(a)], using the simulated tropospheric delay as the reference. The result is shown in Fig. 6(e). Each error bar represents the median absolute error $+/-$ MAD of each acquisition among its ten realizations. The proposed method could reduce the tropospheric delay from a median value of 2.0 (light gray bars)– 0.4 cm (red error bars), which is smaller than the deformation (with a median value of 1.1 cm) and comparable to the tropospheric turbulence (dark gray error bars with a median value of 0.6 cm), as expected, confirming the effectiveness of the texture correlation method to separate the stratified tropospheric delay from deformation in various scenarios. Note that the texture correlation method also outperforms the local linear fitting method (blue error bars with a median value of 0.9 cm), where the latter shows obvious negative situations for several cases with relatively weak tropospheric delays.

C. Impact of the Texture Estimation Window Size

To analyze the impact of estimation window size on the performance of the method, we calculate the median absolute error of the 28×10 simulations with various estimation window sizes in both the deforming region ($\sim$2 $\times$ 1.7 km in size) and the entire region, respectively, as shown in Fig. 6(f) and (g). The results show that the texture correlation method works well with window size larger than 0.6 km, and works the best if the window size is also smaller than 4 km. The steep rise of estimation error for window sizes smaller than 0.6 km should be due to the insufficient texture information within the estimation window. The slow rise of estimation error for window sizes exceeding 4 km in the deforming region [see Fig. 6(f)] is due to the strong tropospheric heterogeneity surrounding the peak topography [with the average elevation marked by the orange vertical dashed line in Fig. 6(g) (inset)], as shown in Fig. 6(g) (inset) for the flattened phase–elevation scatter plot of the ERA5 stratified tropospheric delay. Note the local linear fitting method performs poor in the deforming region, the performance improves as the window size increases, indicating a direct correlation with the percentage of the deforming regions within the estimation window. The good performance in the entire region is due to the small percentage of the deforming region.

V. REAL DATA EXPERIMENTS

We apply the proposed texture correlation method to an ALOS-2 InSAR time series dataset covering the Kirishima volcanic complex of Japan, with typical topography-correlated deformation from the pre-eruptive inflation at Iwo-yama and Shinmoe-dake volcanoes. We compare the proposed method with the model-based method using ERA5 weather reanalysis dataset [8], [40], the phase–elevation fitting methods, including the global linear fitting [17] and the local linear
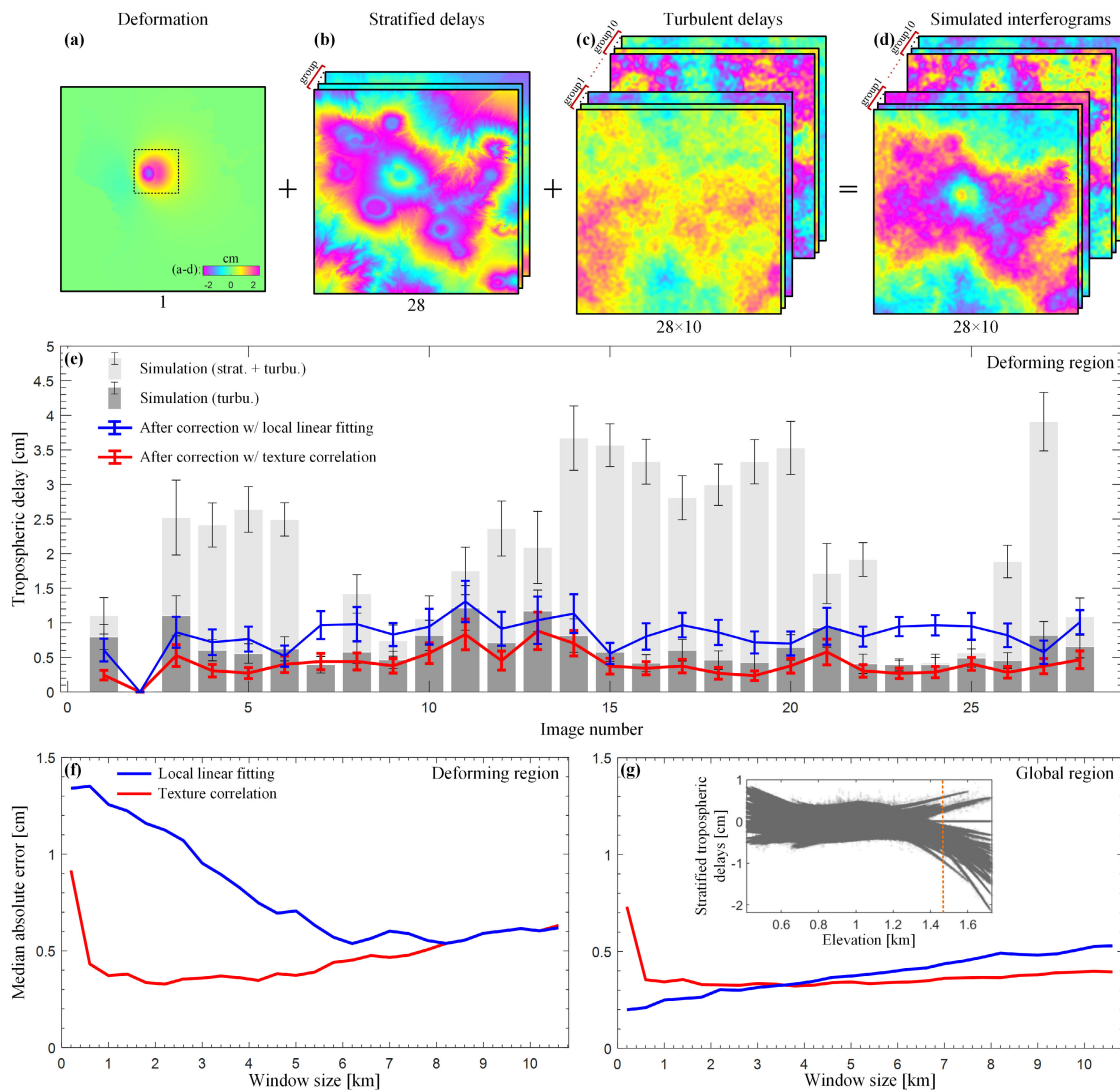
Fig. 6. Data simulation. (a)–(d) Interferometric phase simulation, including (a) surface deformation simulated using the same parameters as the pre-eruptive inflation of the 2017 Shinmoe-dake eruption [35], [36], [37], (b) 28 stratified tropospheric delays from ERA5, which we refer to as a group, (c) ten realizations (groups) of 28 tropospheric turbulence simulated using the power-law behavior [3], [38] with parameters estimated from the real residual phase time series (after removing ERA5 and deformation signals), and (d) sum of (a)–(c). All the data are rewrapped into [−2.5, 2.5) cm for display. (e) Tropospheric delay time series before (light gray error bars) and after corrections using local linear fitting (blue error bars) and texture correlation (red error bars) methods at the deforming region, respectively. Simulated tropospheric turbulence time series are also shown in dark gray error bars. The error bar represents the median absolute error +/− MAD of each acquisition among its ten realizations. Overall tropospheric estimation error as a function of the texture estimation window size at (f) deforming region and (g) global region, respectively. Inset in (g): flattened phase–elevation scatterplot using ERA5 data in (b). For each date, a linear slope is estimated using data with elevations of 700–1300 m and removed from all data, to flatten/align all scatterplots into one. The deforming region is outlined as the black dashed box in (a).

fitting [16], [19]. Note that for the local linear fitting method, we estimate the slope and intercept within each window and then interpolates the two to the whole space. The iterative weighting ("masking") and time function fitting are omitted.

A. Experiment Site and Dataset

The Kirishima volcanic complex, which is known as "foggy mountain" in Japanese, is situated in southern Kyushu, Japan. This complex comprises over 25 craters, cones, and lava domes (see Fig. 2; [41]). The active eruptive centers within the complex include Iwo-yama and Shinmoe-dake, reaching altitudes of 1313 and 1421 m, respectively. Shinmoe-dake erupted in 2011, 2017, and 2018 while Iwo-yama erupted in 2018, all have pre-eruptive inflations observed in InSAR [35].

We use the InSAR time series from L-band ALOS-2 descending track 23 acquired between February 9, 2015 and September 18, 2017 with 28 SAR acquisitions, as provided by Yunjun et al. [35]. The dataset covers a region of $\sim 9 \times 11$ km^2 with a spatial resolution of 0.000185185° (~ 20 m). Topographic residuals due to DEM errors have been corrected [28], and a linear plane has been estimated and removed for each acquisition to mitigate the potential ionospheric delay, the tropospheric delay is not corrected. We refer to the resulting phase time series as the original time series, based on which the proposed method and comparison with other methods are applied.

For the proposed texture correlation method, we set the slope estimation window size W to 141 pixels (~ 2.8 km), with
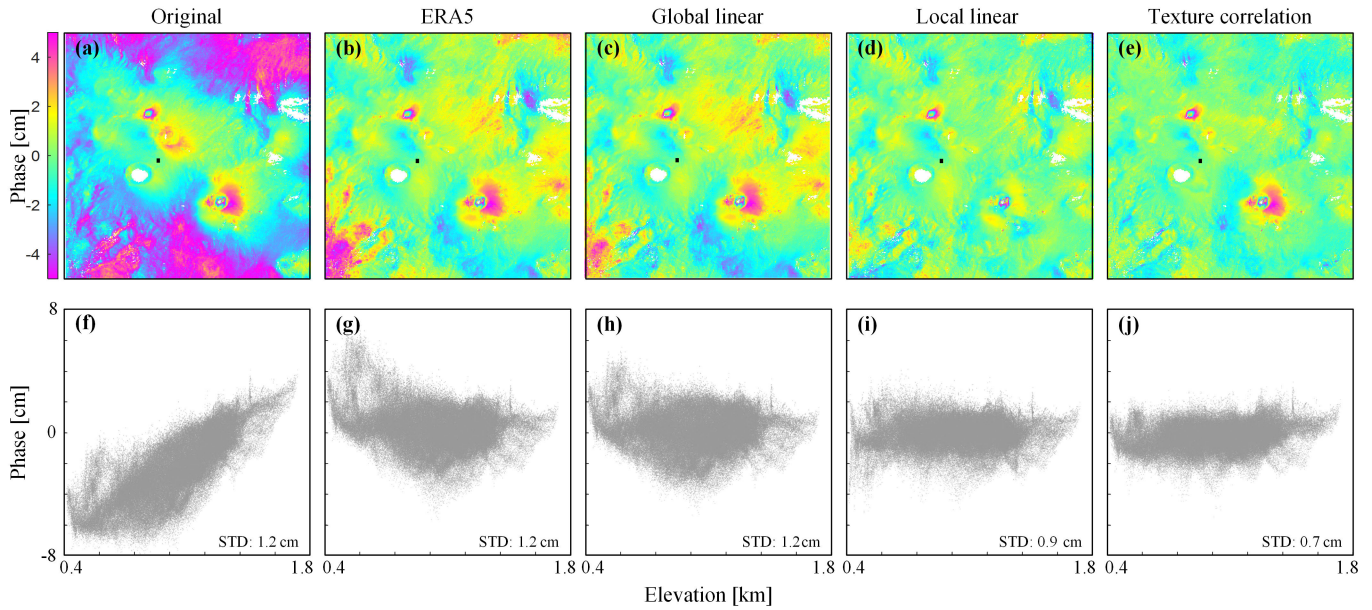
Fig. 7. Comparison on a single interferogram (acquired between February 23, 2015 and August 21, 2017). Unwrapped phase (a) before and after tropospheric correction using (b) ERA5, (c) global linear fitting, (d) local linear fitting, and (e) proposed texture correlation methods. Black squares: reference points. Data are rewrapped into [−5, 5) cm for display. (f)–(j) Phase–elevation scatterplots for each of the unwrapped phases above with deforming areas masked out.

an overlap between adjacent windows of 40%. The intercept filter window size w_d is set to 251 pixels ($\sim$5.0 km), and the slope filter window size w_k is set to 7 pixels. For the local linear fitting method, we use the same window-related parameters.

B. Single Interferogram

We take a single interferogram as an example and show the correction results in Fig. 7. From Fig. 7(a), it can be observed that the original interferogram exhibits significant stratified tropospheric delays, showing a clear correlation with the topography [see Fig. 2(a)] and exhibiting noticeable spatial heterogeneity, such as the bottom-left corner where tropospheric phase does not perfectly correlate with topography. After correction by ERA5 [see Fig. 7(b)], most of the prominent stratified tropospheric delays are removed, highlighting the deformation of the Iwo-yama and Shinmoe-dake volcanoes. However, there are still visible tropospheric delays remaining in the east and southwest regions. The global linear method also brings noticeable improvement [see Fig. 7(c)], similar to ERA5, but with more apparent residual tropospheric delays in the southern region of Shinmoe-dake volcano. Both methods fail to address heterogeneous tropospheric delays. The local linear method [see Fig. 7(d)] allows delicate handling of heterogeneity and provides a better solution than the ERA5 and global linear methods overall. However, the topography-correlated deformation signal at Shinmoe-dake volcano is severely smoothed out, which is expected but unacceptable. The proposed texture correlation method [see Fig. 7(e)] significantly weakens the residual stratified tropospheric delay, even slightly better than the local linear method, while effectively preserving the deformation signal at both active volcanoes.

The phase–elevation scatterplots in Fig. 7 (bottom) further confirm the aforementioned conclusions. Although the global linear method [see Fig. 7(g)] flattens the clear linear phase–elevation relationship in the original interferogram [see Fig. 7(f)], the proposed texture correlation method [see Fig. 7(j)] further abolishes the dependence of the phase on elevation and exhibits the smallest STD among all methods.

C. Deformation Rate and Time Series

The estimated deformation rate from the time series before and after tropospheric corrections is presented in Fig. 8 (top). ERA5 and the global linear method achieve equally favorable results [see Fig. 8(b) and (c)], with clear deformation at Iwo-yama and Shinmoe-dake volcanoes and a little residual tropospheric delays in the northeast and southwest regions. The local linear method significantly reduces the tropospheric noise in nondeforming regions [see Fig. 8(d)], but also distorts the deformation signal at Shinmoe-dake volcano. The proposed texture correlation method obtains deformation patterns similar to ERA5, but with less impact from residual tropospheric delays [see Fig. 8(e)].

Fig. 8(f)–(i) shows the deformation time series of four representative points with different deformation behaviors [marked as f, g, h, i in Fig. 8(a)]: f at Shinmoe-dake volcano with topography-correlated deformation, g at Iwo-yama volcano with topography-uncorrelated deformation, and h and i in the stable region with small and large STDs of the original time series in the time domain, respectively. For deforming point f, given that the selected reference point [black square in Fig. 8(a)] is in close proximity to Shinmoe-dake volcano in both horizontal distance (about 3 km) and vertical elevation (about 80 m), we expect minimal impact from troposphere [27], thus, the original time series can
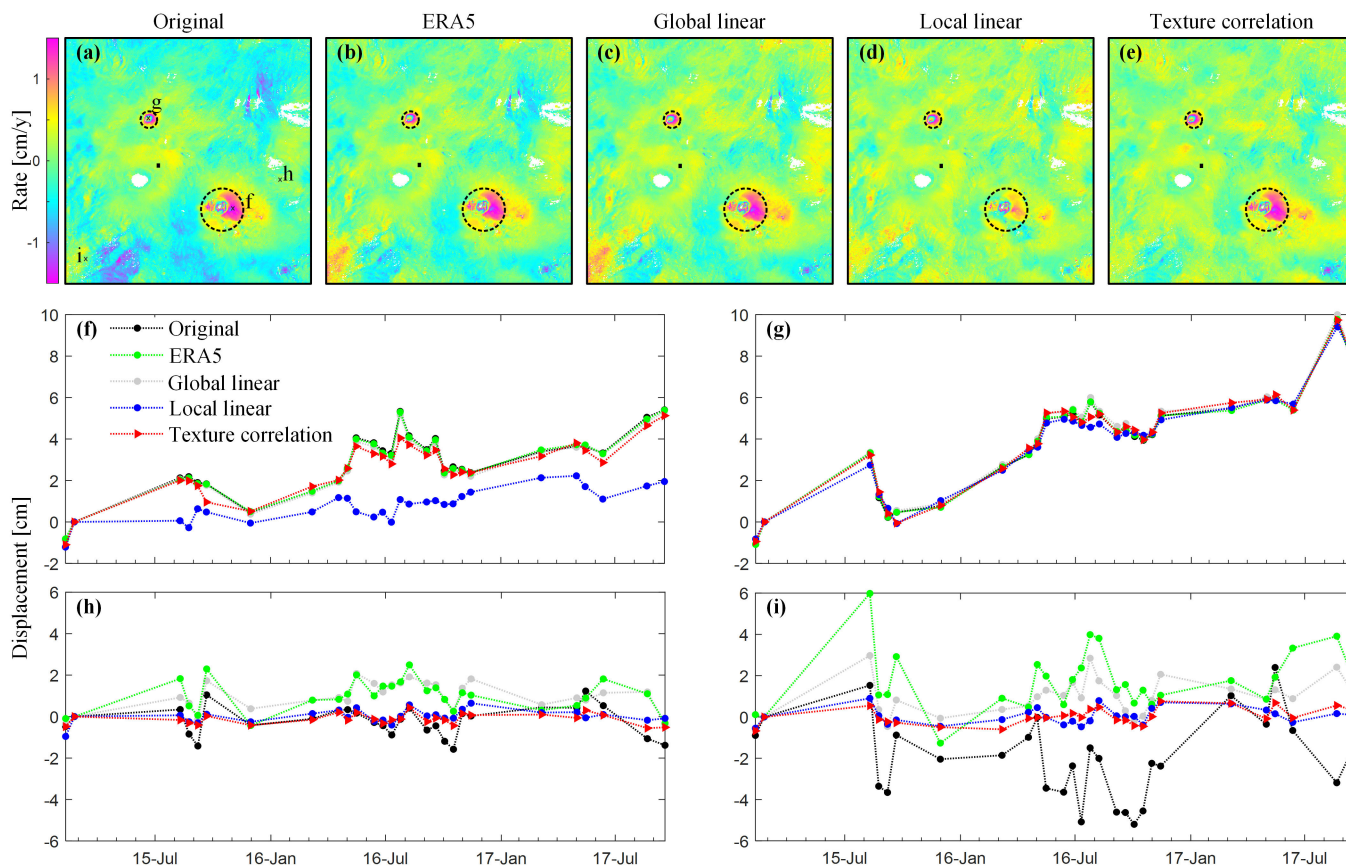
Fig. 8. Comparison of deformation rate and time series before and after correction. (a)–(e) Deformation rate maps calculated from the phase time series before and after the stratified tropospheric correction by different methods, including (a) without correction, (b) ERA5-based method, (c) global linear fitting, (d) local linear fitting, and (e) proposed texture correlation methods. Black squares: reference points. Data are rewrapped into [−1.5, 1.5] cm/year for display. (f)–(i) Deformation time series of four representative points $f - i$ as marked in (a), where points f and g are sampled on the topography-correlated and topography-uncorrelated deformation areas, and points h and i are sampled on the stable area with small and large STDs of the original time series [refer to Fig. 10(a)], respectively. Black, green, gray, blue, and red dashed lines indicate results without correction, with correction using ERA5, global linear, local linear, and the proposed texture correlation method, respectively.
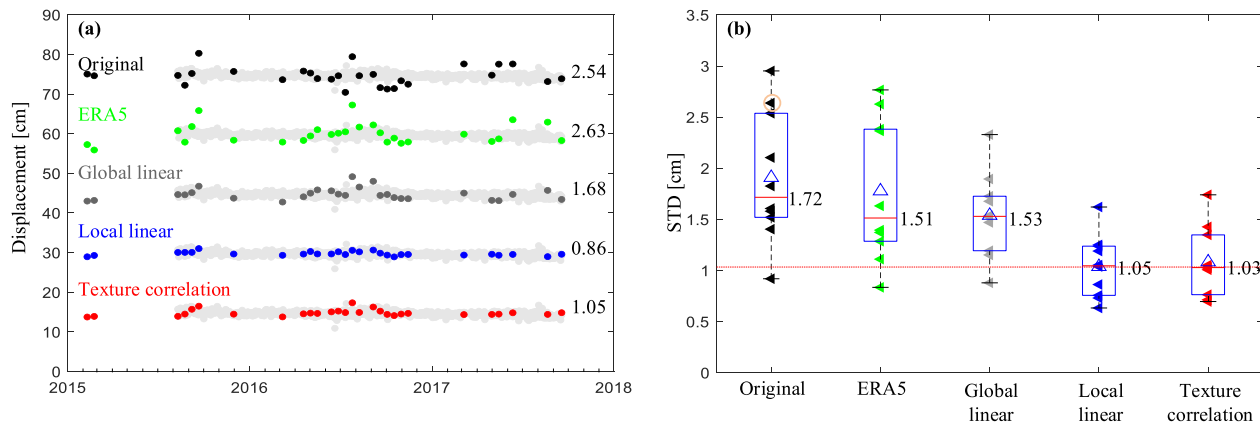

Fig. 9. Comparison with GNSS. (a) Comparison with one GNSS time series pair of J714-X083. Gray dots represent the GNSS daily solutions in the radar LOS direction. Black, green, gray, blue, and red dots represent InSAR time series before and after tropospheric correction using ERA5, global linear fitting, local linear fitting, and the proposed texture correlation methods, respectively. Each GNSS time series is shifted by a constant offset for display, the InSAR time series is shifted by its median difference with the GNSS time series. Numbers on the right are the STD of the differences between InSAR and GNSS LOS displacements. (b) STD statistics among the ten GNSS pairs. Solid triangles represent STD obtained with InSAR time series corrected by different methods. For each method, the central red solid horizontal line indicates the median value, the blue hollow triangle indicates the average value, while the bottom and top edges of the box indicate the 25th and 75th percentiles, respectively. The orange circle marks the GNSS pair shown in (a).

be employed as a reference for the true deformation. The ERA5 correction gives nearly the same result as the original

deformation time series. The global linear method does not make apparent change due to the close elevation between the
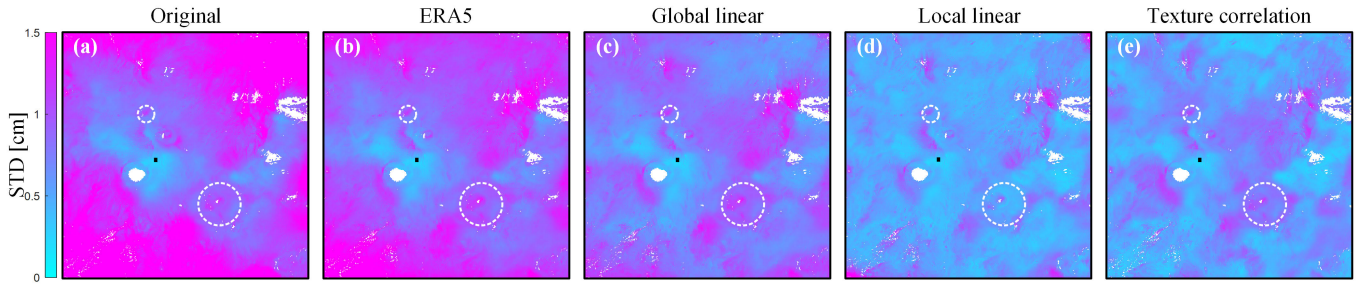
Fig. 10.   Temporal STD of the residual phase time series before and after the tropospheric correction by different methods. (a) Not corrected. Corrected using (b) ERA5, (c) global linear fitting, (d) local linear fitting, and (e) proposed texture correlation methods. Black squares: reference points.
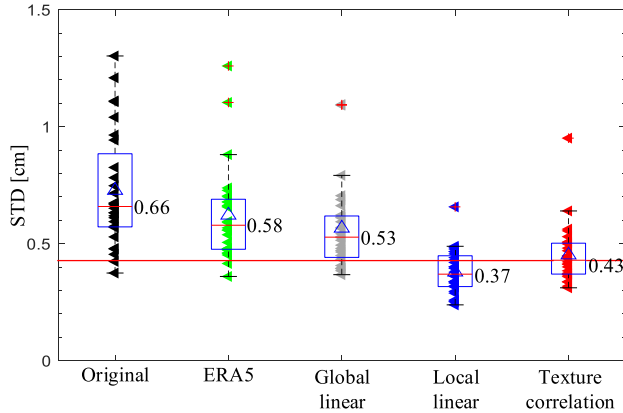

Fig. 11.   Spatial STD of the residual phase time series before and after the stratified tropospheric correction by different methods. Solid triangles: STD of each acquisition. Hollow triangles: average STD. For each method, the central red solid line indicates the median STD, while the bottom and top edges of the box indicate the 25th and 75th percentiles, respectively.

reference point and f, which have almost the same correction prediction from the method. The local linear method shows its limitations in such cases of topography-related deformation, because the estimation is heavily interfered by the deformation signals. While the texture correlation method, also as a localized method, gives result that is very close to the original phase time series due to the much lower sensitivity to the deformation signal. For topography-uncorrelated deforming points g, all methods gave consistent results. For stable points h and i, the texture correlation method together with the local linear method makes the deformation time series converge to 0. And at this point, nonlocal methods such as ERA5 and global linear show their limitations.

VI. Discussion

We further evaluate the method using external GNSS data and statistics of the residual phase, and discuss the two assumptions of the proposed method as well as its limitations.

A. Comparison With GNSS

We use five publicly available GNSS stations from the University of Nevada at Reno [42] (X083, G087, J714, X082, and J486; check Fig. 2(b) for detailed locations), which form ten differential GNSS displacement time-series pairs. All

sites are far away from the local deformation at Shinmoe-dake and Iwo-yama volcanoes, unfortunately. We project the east, north and up GNSS displacement into the radar line of sight (LOS) direction, then shift each InSAR time series by its median difference with the GNSS LOS time series for comparison. Fig. 9(a) shows the comparison between GNSS and InSAR time series before and after the four tropospheric corrections at GNSS site pair J714-X083. All methods improve the agreement between InSAR and GNSS, except for ERA5, which worsen the agreement slightly. The texture correction and local linear methods give the best agreement.

Fig. 9(b) shows the statistics among all ten pairs of time-series. Assuming GNSS displacement as the truth, we can see that all methods reduce the STD. Both ERA5 and global linear methods reduce the median STD from 1.7 to 1.5 cm, while the local linear and texture correlation methods show similar performance with the texture correlation method having the smallest median STD of 1.0 cm by only a small margin.

B. Performance Assessment Using Temporal and Spatial Standard Deviation of Residual Phase

We evaluate the performance of tropospheric corrections using the temporal and spatial STD of the residual phase, which has been corrected for the ionosphere and deformation using a quadratic polynomial time function. Fig. 10 shows the temporal STD maps of different correction methods. The temporal STD of the original time series is high over a large area, which is expected. Although the effectiveness of ERA5 has been well illustrated before, the temporal STD does not change much after correction, indicating limited performance in the time domain. Compared with ERA5, the global linear method shows noticeable improvements overall [see Fig. 10(c)], demonstrating the advantages of the phase-based approach over the external-data-based approach in capturing the temporal variation of tropospheric delays, at least for this dataset. The local linear method shows similar performance as in Section V-B, while significantly reducing residual tropospheric delays, it fails to capture the highly nonlinear deformation and smooths out the deforming areas with an abnormally low temporal STD at Shinmoe-dake volcano [see Fig. 10(d)]. In contrast, the texture correlation method achieves the small overall temporal STD second only to the local linear method at stable areas and the expected high temporal STD at deforming areas.
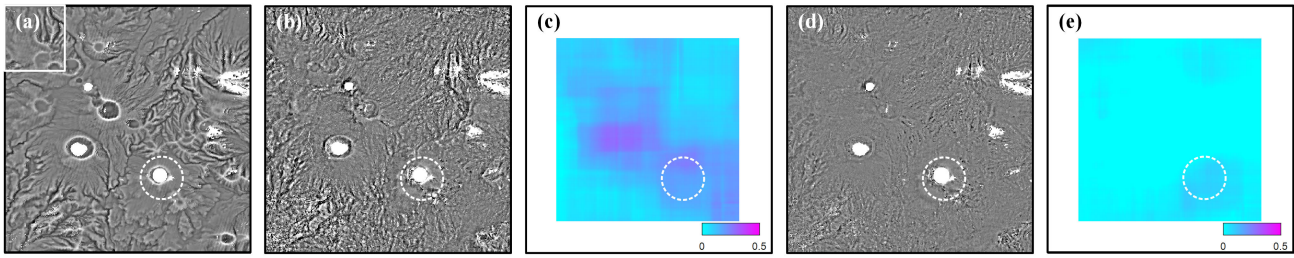
Fig. 12. Maps of textures and the correlation coefficients between them. (a) and (b) Texture maps for topography and interferogram (February 23, 2015 and August 21, 2017), respectively. (c) Correlation coefficient map between (a) and (b). (d) and (e) Same as (b) and (c) but for the deformation rate [obtained by the proposed method, as shown in Fig. 8(e)]. The white box in (a) indicates the window size for correlation calculation (141 × 141 pixels, ~2.8 × 2.4 km), and the white dashed circles indicate the extent of topography-correlated deformation. Note that the correlation coefficients for regions with fewer than 141 × 141 pixels in the estimation window near the edge in (c) and (e) are not displayed.

For the spatial STD, we mask out the deforming areas and evaluate the statistics of the calculated spatial STD time series in Fig. 11. After ERA5 correction, the median spatial STD reduces 12% from 0.66 to 0.58 cm, while the global linear, local linear, and texture correlation methods provide an STD reduction of 20%, 44%, and 35%, respectively, highlighting the superiority of local window estimation, especially the texture correlation method, which brings the median spatial STD down to 0.43 cm. Note that abnormal statistical value originates from strong tropospheric turbulence in SAR interferogram acquired between February 23, 2015 and August 10, 2015 with our reference point, which can be clearly seen in [35, Fig. S8].

C. Assumptions and Limitations

We discuss the validity of assumptions and potential limitations of our proposed method. The first assumption is the weak texture correlation between deformation and topography (from the low-resolution stratified tropospheric estimation module in Section III-A). Fig. 12 shows full-scale maps of the texture correlation between deformation rate, an example interferogram, and topography (small-scale high-rate deformation areas are masked out in advance before the correlation calculation). It is evident that the texture correlation between the deformation and topography [see Fig. 12(e)] is much lower than that between the interferogram and topography [see Fig. 12(c)]. Even at Shinmoe-dake (dashed white circle), where a topography-correlated deformation occurs and the topography texture is not rich, the texture correlation between deformation and topography is still lower, confirming the feasibility of the assumption. And in the case where a local deformation is somewhat correlated with topography in the texture domain, the low-pass filtering of the phase–elevation slope as in (5) could further mitigate this local-scale impact.

The second assumption is that deformation is not correlated with the tropospheric phase–elevation slope in the temporal high-frequency component (from the high-resolution tropospheric delay correction module in Section III-B). Fig. 13 shows the estimated phase–elevation slope from the ERA5 prediction, the proposed texture correlation method, and its temporal high-frequency component. The sinusoidal behavior of the ERA5 slope coincides with the nature of seasonal oscillations in the stratified tropospheric delay. The slope oscillation pattern from the texture correlation method is approximately
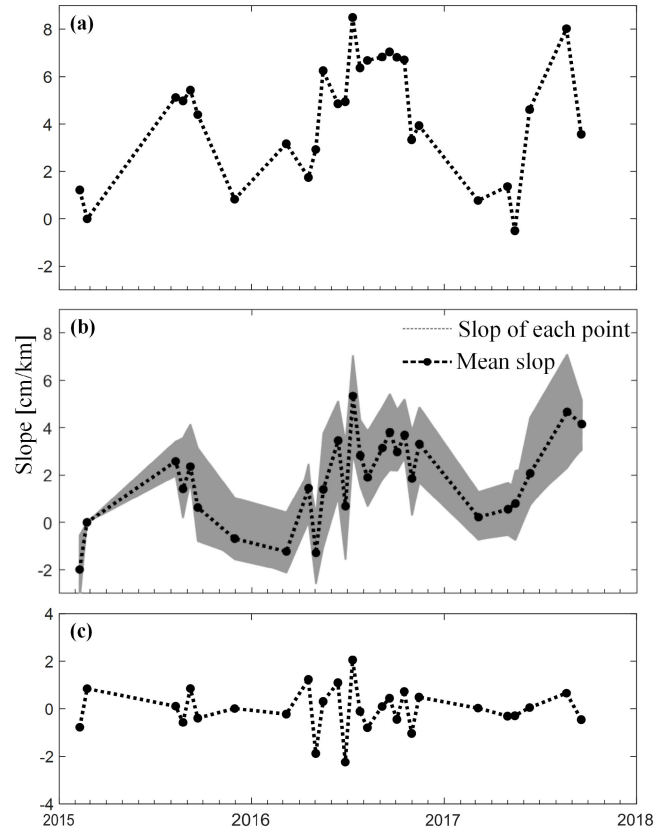

Fig. 13. Phase–elevation slope time series of stratified tropospheric delays estimated from (a) ERA5 delays prediction, (b) proposed texture correlation method (see Section III-A), and (c) temporal high-frequency component of (b). For (b), the thin gray dashed lines are the slope estimates of 89 × 89 points sampled uniformly at 5-pixel intervals in the nonedge region of the interferogram, with the thick black dashed line marked with black circles as the mean value.

consistent with the independent ERA5 prediction, with a correlation coefficient of 0.73. The temporal high-frequency component of the texture correlation slope [see Fig. 13(c)] appears to be random in time, thus unlikely to be correlated with the one of deformation except with a bad reference point. A sufficiently long temporal coverage of SAR data is recommended for a robust inversion of (13). Nevertheless, if the condition for the second assumption is not satisfied, one can discard the high-resolution stratified tropospheric correction and retain only the result from the low-resolution stratified tropospheric estimation.

Last but not least, there is a limitation to the proposed method: it cannot be applied to datasets with significant portions of deforming areas, such as the large spatial wavelength deformation from tectonic processes, or local-scale deformation but with a relatively large coverage (resulting in a large portion of deforming areas), because the intercept filtering step will inevitably smooth out the deformation signal.

VII. CONCLUSION

We present a new phase-based method to estimate and correct for the heterogeneous stratified tropospheric delay in InSAR data. The method uses the high-frequency texture correlation at local estimation windows, thus, is able to capture the heterogeneous troposphere with the presence of local-scale topography-correlated deformation. The method is built upon two assumptions: 1) deformation is weakly correlated with topography in the texture domain and 2) deformation is not correlated with tropospheric phase–elevation slope in the temporal high-frequency component. Both assumptions are easy to meet in practice. We apply the method to ALOS-2 data over Kirishima volcanic complex in Japan. The proposed method reduces the median spatial STD of the residual phase from 0.66 to 0.43 cm, which is smaller than the value from using ERA5, global linear fitting, showing superior performance without compromising the deformation signal.

REFERENCES

[1] M. Simons and P. A. Rosen, *3.12—Interferometric Synthetic Aperture Radar Geodesy*, vol. 3. Oxford, U.K.: Elsevier, 2015, pp. 339–385.

[2] H. A. Zebker and J. Villasenor, "Decorrelation in interferometric radar echoes," *IEEE Trans. Geosci. Remote Sens.*, vol. 30, no. 5, pp. 950–959, Sep. 1992.

[3] R. F. Hanssen, *Radar Interferometry: Data Interpretation and Error Analysis*, vol. 2. Dordrecht, The Netherlands: Kluwer Academic, 2001.

[4] Z. Yunjun, H. Fattahi, and F. Amelung, "Small baseline InSAR time series analysis: Unwrapping error correction and noise reduction," *Comput. Geosci.*, vol. 133, Dec. 2019, Art. no. 104331.

[5] D. P. S. Bekaert, A. Hooper, and T. J. Wright, "A spatially variable power law tropospheric correction technique for InSAR data," *J. Geophys. Res., Solid Earth*, vol. 120, no. 2, pp. 1345–1356, Feb. 2015.

[6] H. Fattahi and F. Amelung, "InSAR bias and uncertainty due to the systematic and stochastic tropospheric delay," *J. Geophys. Res., Solid Earth*, vol. 120, no. 12, pp. 8758–8773, Dec. 2015.

[7] T. R. Emardson, M. Simons, and F. H. Webb, "Neutral atmospheric delay in interferometric synthetic aperture radar applications: Statistical description and mitigation," *J. Geophys. Res., Solid Earth*, vol. 108, no. B5, pp. 2231–2238, May 2003.

[8] R. Jolivet, R. Grandin, C. Lasserre, M.-P. Doin, and G. Peltzer, "Systematic InSAR tropospheric phase delay corrections from global meteorological reanalysis data," *Geophys. Res. Lett.*, vol. 38, no. 17, pp. 1–5, Sep. 2011.

[9] R. Jolivet et al., "Improving InSAR geodesy using global atmospheric models," *J. Geophys. Res., Solid Earth*, vol. 119, no. 3, pp. 2324–2341, Mar. 2014.

[10] C. Yu, Z. Li, N. T. Penna, and P. Crippa, "Generic atmospheric correction model for interferometric synthetic aperture radar observations," *J. Geophys. Res., Solid Earth*, vol. 123, no. 10, pp. 9202–9222, Oct. 2018.

[11] Y. Cao, S. Jònsson, and Z. Li, "Advanced InSAR tropospheric corrections from global atmospheric models that incorporate spatial stochastic properties of the troposphere," *J. Geophys. Res., Solid Earth*, vol. 126, no. 5, May 2021, Art. no. e2020JB020952.

[12] J. Maurer et al., "RAiDER: Raytracing atmospheric delay estimation for RADAR," in *Proc. AGU Fall Meeting Abstr.*, 2021, p. 44.

[13] Z. Li, E. J. Fielding, P. Cross, and R. Preusker, "Advanced InSAR atmospheric correction: MERIS/MODIS combination and stacked water vapour models," *Int. J. Remote Sens.*, vol. 30, no. 13, pp. 3343–3363, Jul. 2009.

[14] F. Onn and H. A. Zebker, "Correction for interferometric synthetic aperture radar atmospheric phase artifacts using time series of zenith wet delay observations from a GPS network," *J. Geophys. Res.: Solid Earth*, vol. 111, no. B9, Sep. 2006, Art. no. B09102.

[15] C. Yu, Z. Li, and N. T. Penna, "Interferometric synthetic aperture radar atmospheric correction using a GPS-based iterative tropospheric decomposition model," *Remote Sens. Environ.*, vol. 204, pp. 109–121, Jan. 2018.

[16] H. Liang, L. Zhang, Z. Lu, and X. Li, "Correction of spatially varying stratified atmospheric delays in multitemporal InSAR," *Remote Sens. Environ.*, vol. 285, Feb. 2023, Art. no. 113382.

[17] M.-P. Doin, C. Lasserre, G. Peltzer, O. Cavalié, and C. Doubre, "Corrections of stratified tropospheric delays in SAR interferometry: Validation with global atmospheric models," *J. Appl. Geophys.*, vol. 69, no. 1, pp. 35–50, Sep. 2009.

[18] K. D. Murray, R. B. Lohman, and D. P. S. Bekaert, "Cluster-based empirical tropospheric corrections applied to InSAR time series analysis," *IEEE Trans. Geosci. Remote Sens.*, vol. 59, no. 3, pp. 2204–2212, Mar. 2021.

[19] Y. Wang et al., "Refined InSAR tropospheric delay correction for wide-area landslide identification and monitoring," *Remote Sens. Environ.*, vol. 275, Jun. 2022, Art. no. 113013.

[20] Y. N. Lin, M. Simons, E. A. Hetland, P. Muse, and C. DiCaprio, "A multiscale approach to estimating topographically correlated propagation delays in radar interferograms," *Geochem., Geophys., Geosyst.*, vol. 11, no. 9, pp. 2–17, Sep. 2010.

[21] E. Tymofyeyeva and Y. Fialko, "Mitigation of atmospheric phase delays in InSAR data, with application to the eastern California shear zone," *J. Geophys. Res., Solid Earth*, vol. 120, no. 8, pp. 5952–5963, Aug. 2015.

[22] M. S. Zebker, J. Chen, and M. A. Hesse, "Robust surface deformation and tropospheric noise characterization from common-reference interferogram subsets," *IEEE Trans. Geosci. Remote Sens.*, vol. 61, 2023, Art. no. 5210914.

[23] F. Albino, J. Biggs, and D. K. Syahbana, "Dyke intrusion between neighbouring arc volcanoes responsible for 2017 pre-eruptive seismic swarm at Agung," *Nature Commun.*, vol. 10, no. 1, p. 748, Feb. 2019.

[24] G. Castellano, L. Bonilha, L. M. Li, and F. Cendes, "Texture analysis of medical images," *Clin. Radiol.*, vol. 59, no. 12, pp. 1061–1069, Dec. 2004.

[25] E. Chapin et al., "Impact of the ionosphere on an L-band space based radar," in *Proc. IEEE Conf. Radar*, Apr. 2006, pp. 1–8.

[26] G. Gomba, A. Parizzi, F. De Zan, M. Eineder, and R. Bamler, "Toward operational compensation of ionospheric effects in SAR interferograms: The split-spectrum method," *IEEE Trans. Geosci. Remote Sens.*, vol. 54, no. 3, pp. 1446–1461, Mar. 2016.

[27] E. Chaussard, E. Havazli, H. Fattahi, E. Cabral-Cano, and D. Solano-Rojas, "Over a century of sinking in Mexico city: No hope for significant elevation and storage capacity recovery," *J. Geophys. Res., Solid Earth*, vol. 126, no. 4, Apr. 2021, Art. no. e2020JB020648.

[28] H. Fattahi and F. Amelung, "DEM error correction in InSAR time series," *IEEE Trans. Geosci. Remote Sens.*, vol. 51, no. 7, pp. 4249–4259, Jul. 2013.

[29] H. Fattahi and F. Amelung, "InSAR uncertainty due to orbital errors," *Geophys. J. Int.*, vol. 199, no. 1, pp. 549–560, Jul. 2014.

[30] Q. Yang et al., "Image-based baseline correction method for spaceborne InSAR with external DEM," *IEEE Trans. Geosci. Remote Sens.*, vol. 61, 2023, Art. no. 5202216.

[31] P. Marinkovic and Y. Larsen, "Consequences of long-term ASAR local oscillator frequency decay—An empirical study of 10 years of data," in *Proc. Living Planet Symp.*, 2013.

[32] C. J. DiCaprio and M. Simons, "Importance of ocean tidal load corrections for differential InSAR," *Geophys. Res. Lett.*, vol. 35, no. 22, pp. 581–592, Nov. 2008.

[33] Z. Yunjun et al., "Range geolocation accuracy of C-/L-band SAR and its implications for operational stack coregistration," *IEEE Trans. Geosci. Remote Sens.*, vol. 60, 2022, Art. no. 5227219.

[34] H. Liang, L. Zhang, X. Ding, Z. Lu, and X. Li, "Toward mitigating stratified tropospheric delays in multitemporal InSAR: A quadtree aided joint model," *IEEE Trans. Geosci. Remote Sens.*, vol. 57, no. 1, pp. 291–303, Jan. 2019.

[35] Z. Yunjun, F. Amelung, and Y. Aoki, "Imaging the hydrothermal system of Kirishima volcanic complex with L-band InSAR time series," *Geophys. Res. Lett.*, vol. 48, no. 11, Jun. 2021, Art. no. e2021GL092879.

[36] M. Nikkhoo, T. R. Walter, P. R. Lundgren, and P. Prats-Iraola, "Compound dislocation models (CDMs) for volcano deformation analyses," *Geophys. J. Int.*, vol. 208, no. 2, pp. 877–894, Feb. 2017, doi: 10.1093/gji/ggw427.

[37] C. A. Williams and G. Wadge, "The effects of topography on magma chamber deformation models: Application to Mt. Etna and radar interferometry," *Geophys. Res. Lett.*, vol. 25, no. 10, pp. 1549–1552, May 1998.

[38] Z. Yunjun, H. Fattahi, P. Agram, P. Rosen, and M. Simons, "InSAR uncertainty due to phase unwrapping errors," in *Proc. AGU Fall Meeting Abstr.*, 2020, p. 23.

[39] E. A. Hetland, P. Musé, M. Simons, Y. N. Lin, P. S. Agram, and C. J. DiCaprio, "Multiscale InSAR time series (MInTS) analysis of surface deformation," *J. Geophys. Res., Solid Earth*, vol. 117, no. B2, pp. 1–17, Feb. 2012.

[40] H. Hersbach et al., "The ERA5 global reanalysis," *Quart. J. Roy. Meteorological Soc.*, vol. 146, no. 730, pp. 1999–2049, 2020.

[41] S. Nakada, M. Nagai, T. Kaneko, Y. Suzuki, and F. Maeno, "The outline of the 2011 eruption at Shinmoe-dake (Kirishima), Japan," *Earth, Planets Space*, vol. 65, pp. 475–488, Jun. 2013.

[42] G. Blewitt, W. Hammond, and C. Kreemer, "Harnessing the GPS data explosion for interdisciplinary science," *Eos*, vol. 99, p. 485, Sep. 2018.

Qingyue Yang (Graduate Student Member, IEEE) was born in Shaanxi, China, in 1997. She received the B.S. degree in electronic engineering from Xidian University, Xi'an, China, in 2019. She is currently pursuing the Ph.D. degree with the National Key Laboratory of Microwave Imaging Technology, Aerospace Information Research Institute, Chinese Academy of Sciences, Beijing, China.

She is also with the University of Chinese Academy of Sciences, Beijing. Her research interests include InSAR, TS-InSAR signal processing, and their application in DEM generation and surface deformation detection.

Zhang Yunjun (Member, IEEE) received the B.Eng. degree in remote sensing from Wuhan University, Wuhan, China, in 2011, the M.Sc. degree in geodesy from the University of Chinese Academy of Sciences, Beijing, China, in 2014, and the Ph.D. degree in geophysics from the University of Miami, Miami, FL, USA, in 2019.

He was a Post-Doctoral Scholar with the Seismological Laboratory, California Institute of Technology, Pasadena, CA, USA, where he was also involved with the Observational Products for End-users using Remote sensing Analysis (OPERA) project of the Jet Propulsion Laboratory, from 2019 to January 2023. Since then, he has been with the Aerospace Information Research Institute, Chinese Academy of Sciences, Beijing, where he is currently a Professor of electrical engineering. His research interests include algorithm and tools development for SAR, InSAR, and their time-series analysis, and solid Earth processes associated with active volcanism, tectonics, and geohazards.

Robert Wang (Senior Member, IEEE) received the B.S. degree in control engineering from the University of Henan, Kaifeng, China, in 2002, and the Dr.Eng. degree from the Graduate University of Chinese Academy of Sciences, Beijing, China, in 2007.

He was with the Center for Sensor Systems (ZESS), University of Siegen, Siegen, Germany, from 2007 to 2011, where he was involved in various joint projects supported by ZESS and Fraunhofer-FHR, Wachtberg, Germany. Since 2011, he has been with the Aerospace Information Research Institute, Chinese Academy of Sciences (CAS), Beijing, where he is currently the Director of the National Key Laboratory of Microwave Imaging Technology and a Co-Principal Investigator with the Helmholtz-CAS Joint Research Group, Beijing. He is the Radar Payload Principal Investigator of the LuTan-1 mission and is responsible for several high-resolution spaceborne imaging radar missions supported by the National High-Resolution Earth Observation Major Special Program. He has authored more than 100 peer-reviewed journal articles and one book. His research interests include monostatic/multistatic SAR imaging and high-resolution wide-swath spaceborne SAR systems and imaging models.

Dr. Wang currently serves as an Associate Editor for the IEEE TRANSACTIONS ON GEOSCIENCE AND REMOTE SENSING.